Insights into the reactive sintering and separated specific grain/grain boundary conductivities of $Li_{1.3}Al_{0.3}Ti_{1.7}(PO_4)_3$

Qi Xu[a,b], Chih-Long Tsai[a], Dongsheng Song[c], Shibabrata Basak[a], Hans Kungl[a], Hermann Tempel[a], Florian Hausen[a,b], Shicheng Yu[a,] and Rüdiger-A. Eichel[a,b,d]*

[a]Institut für Energie– und Klimaforschung (IEK–9: Grundlagen der Elektrochemie), Forschungszentrum Jülich, D–52425 Jülich, Germany

[b]Institut für Physikalische Chemie, RWTH Aachen University, D–52074 Aachen, Germany

[c]Ernst Ruska-Centrum für Mikroskopie und Spektroskopie mit Elektronen (ER-C), Forschungszentrum Jülich, D–52425 Jülich, Germany

[d]Institut für Energie– und Klimaforschung (IEK–12: Helmholtz–Institute Münster, Ionics in Energy Storage), Forschungszentrum Jülich, D–48149 Münster, Germany

*Corresponding author. E-mail: s.yu@fz-juelich.de

Abstract

$Li_{1.3}Al_{0.3}Ti_{1.7}(PO_4)_3$ (LATP) is a promising candidate as solid electrolyte and Li^+ conductive component in the composite electrodes of all-solid-state Li-ion batteries. For both applications, reducing the sintering temperature of LATP while preserving its electrochemical properties is highly desired. This work is dedicated to reducing the sintering temperature of LATP from conventionally around 1000 °C to a low temperature of 775 °C with adding an extra 10 wt. % of Li_2CO_3 to the precursors by a reactive sintering process. Comparative investigations with the stoichiometric LATP prepared by the same sintering method indicate that the combination effect of reactive sintering and Li_2CO_3-excess promotes the liquid phase sintering within LATP which

yielding a high relative density of 95.3 %, whereas the stoichiometric LATP can only achieve a comparable relative density at 875 °C. Furthermore, the reactive sintering assisted Li_2CO_3-excess LATP exhibits a significantly higher ionic conductivity of 0.65 mS cm^{-1} at 25 °C and lower total activation energy of 0.334 eV compared with that of the stoichiometric LATP. Correlative studies on the microstructure and the separated specific grain/grain boundary conductivities for the two samples reveal that the improvement of Li^+ conductivity for Li-excess LATP is attributed to its smaller total grain boundary thickness.

Keywords: LATP solid electrolyte; liquid phase reactive sintering; specific grain boundary conductivity; grain boundary thickness

1. Introduction

Replacing the organic liquid electrolytes in conventional Li-ion batteries by solid electrolytes has motivated substantial interest in developing inorganic fast Li-ion conductors with the concerns of improving safety, and achieving high energy and power densities simultaneously [1]. In recent studies, massive attention has been paid on the sulfide-based (e.g. $Li_{10}GeP_2S_{12}$ and $Li_7P_3S_{11}$ [2,3]), oxide-based (e.g. perovskites-type $Li_{3x}La_{2/3-x}TiO_3$ [4] and garnet-type $Li_7La_3Zr_2O_{12}$ [5,6]) and phosphate-based (e.g. NASICON-type $Li_{1+x}Al_xTi_{2-x}(PO_4)_3$ (LATP) [7,8]) solid electrolytes because of their high ionic conductivities. Compared with sulfide-based solid electrolytes, oxide-based and phosphate-based electrolytes are favorable for practical applications due to their better stability against the ambient atmosphere [9–11].

Among the oxide-based and phosphate-based solid electrolytes, LATP manifests itself from its high ionic conductivity at room temperature (0.1 ~ 1.0 mS cm^{-1}), easy access of raw materials, relative stable in chemistry in ambient atmosphere and advanced mechanical strength (150 MPa)

[12–14]. Nevertheless, the commercialization of high-performance all-solid-state batteries using LATP solid electrolyte is still facing many challenges. Firstly, even though the grain conductivity of LATP (2 ~ 5 mS cm^{-1} at room temperature) [15–17] is sufficient for practical operation of all-solid-state batteries, its total conductivity is usually unsatisfied due to the lower relative densities of the bulk samples from inadequate sintering condition [18] and/or unsatisfactory grain and grain boundary conditions, for instance, non-optimal grain size and impurities at grain boundary [19,20]. Secondly, similar to most ceramic solid electrolytes, the insufficient interfacial connections between LATP and the electrodes result in a large interfacial resistance [21]. In short, improvements of solid-solid particle connections in bulk LATP and between LATP and active electrode materials are prerequisites for the realization of all-solid-state batteries with LATP.

Typically, the sintering temperature of LATP should be 1000 °C or above in order to achieve high bulk density and appropriate ionic conductivity [7,22,23]. On the other hand, sufficient solid-solid interfacial connections can be generated by co-sintering LATP and active materials [24]. Unfortunately, the two approaches contradict as the elevated sintering temperature of LATP causes elemental inter-diffusion and thermally activated side reactions between the solid components in all-solid-state batteries. Kato *et al.* reported the thermal stability of $LiNi_{1/3}Co_{1/3}Mn_{1/3}O_2$ film with a thin LATP sheet at the co-sintering temperatures of 700 °C and 900 °C [25]. The interfacial resistance was 315 Ω cm^2 for the 700 °C sintered sample, which is comparable with that measured using the liquid electrolyte. However, the interfacial resistance dramatically increased by three orders of magnitudes when the components were sintered at 900 °C, due to the formation of lithium-free impurities at the interface [25]. Hence, densified LATP at low sintering temperatures but preserving its high conductivity is essential for the realization of co-sintering LATP with active electrode materials.

The sintering temperature of LATP is greatly dependent on its synthesis and sintering method, as well as the calcination temperature of the precursor. Different solid-state and wet chemical synthesizing approaches along with a variety of heat treatment techniques are developed for low-temperature sintering of LATP. In particular, cold sintering of LATP attracts a lot of attention due to its extraordinary low sintering temperature. Liu *et al*. have extensively discussed about the sintering conditions, solution effects and applied pressure during the cold sintering of LATP [26]. Eventually, highly densified LATP was obtained by an acid-assisted and pressurized cold sintering process. Post annealing of the cold sintered samples at 650 °C were demonstrated to be helpful for improving the total ionic conductivity due to increased crystallinity and phase purity. However, despite the greatly reduced sintering temperature, the obtained LATP exhibits a relative low ionic conductivity about 0.01 mS cm^{-1} at 25 °C compared with the conductivities of LATP prepared by conventional methods [18,19] due to its inherent high total grain boundary resistance that resulted from a large number of grain boundaries and incongruent dissolution of constituent elements in the cold sintering solution [27]. Besides, Hallopeau *et al*. have reported a novel sintering method of microwave-assisted reactive sintering of LATP by which LATP can be prepared in 10 min at a sintering temperature of 890 °C [28]. However, the obtained LATP pellet showed a limited total ionic conductivity of 0.315 mS cm^{-1} at 25 °C due to its low relative density (88 %). Thus, a modified conventional synthesizing and sintering approaches for LATP may be more suitable in concerns of low-temperature sintering of LATP while remaining its competitive ionic conductivity and productivity. In addition to employing a suitable synthesis and sintering method, the calcination temperatures of LATP must be chosen properly since the compositional and morphological characteristics of the calcined precursor powders have a great influence on their sintering behaviors [29]. Full crystallization of LATP requires a calcination temperature above

750 °C [29]. Lower calcination temperatures lead to the existence of intermediate phases. Further higher temperature treatment of the green body made from these intermediate phases results in the formation of LATP with simultaneous densification. This sintering process involving chemical reactions is known as reactive sintering [30,31]. He *et al.* found that by applying reactive sintering of the 600 °C calcined precursor powders, the prepared LATP possesses an appropriate relative density around 91 % and an ionic conductivity of 0.15 mS cm^{-1} at 30 °C [32].

Apart from the preparation method and calcination temperature, additional low melting point sintering additives may help in reducing the sintering temperature of LATP. The working principle of using a sintering additive is to take advantage of the higher diffusion rate of elements in the liquid phase during sintering [33] With the help of sintering additive $CO(NH_2)_2$, Liu *et al.* obtained denser LATP ceramic at the sintering temperature of 800 °C with an improved ionic conductivity of 0.70 mS cm^{-1} at 25 °C compared with that of the sample without sintering additive (0.49 mS cm^{-1} at 25 °C) [34]. However, inducing large amount of less-conductive sintering aids may hinder the transportation of Li^+ between LATP grains. Waetzig *et al.* reported the impact of different sintering aids on the sinterability of LATP [35]. They observed that adding 15 mol % Li_3BO_3 to the 700 °C calcined LATP powders significantly reduced the sintering temperature of LATP to 730 °C, while a relative density of ~93 % was achieved. Conversely, as a consequence of inhomogeneous distribution of the less-conductive sintering aid between the LATP grains, the sample treated with Li_3BO_3 exhibits an ionic conductivity of 0.098 mS cm^{-1} at room temperature, which is almost 4 times lower compared with that of the LATP sintered at 1080 °C without sintering aids [35]. Hence, with the purpose of reducing the sintering temperature of LATP while preserving its high ionic conductivity, the choice of sintering additives along with their amount and method have to be carefully considered.

In the present work, a solid-state-reaction synthesis route by low temperature reactive sintering was used to fabricate LATP. Without compromising the ionic conductivity, the sintering temperature of the stoichiometric LATP (denoted as stoi-LATP) can be reduced to 875 °C by a low temperature calcination of the LATP precursor powders at 600 °C. Further reduction of sintering temperature to 775 °C was achieved by means of adding additional 10 wt. % Li_2CO_3 to the precursors of LATP (denoted as exc-LATP). Here, the excess Li_2CO_3 served as a sintering additive and, on the other hand, compensated the Li^+ loss during sintering. Eventually, the sintering behaviors, structural properties, grain and grain boundary ionic conductivities of stoi-LATP and exc-LATP were investigated and compared systematically.

2. Experimental

2.1. Synthesis of the LATP solid electrolytes

Stoichiometric and Li_2CO_3-excess intermediate LATP powders were prepared by intensively mixing of the precursors followed with low-temperature calcination at 600 °C. Firstly, stoichiometric amount or 10 wt. % excess of Li_2CO_3 (99 %, Sigma-Aldrich) were mixed with stoichiometric amount of Al_2O_3 (99 %, Sigma-Aldrich), TiO_2 (99 %, Sigma-Aldrich) and $NH_4H_2PO_4$ (99 %, Sigma-Aldrich) in a Teflon ball milling container. Absolute isopropanol (99.9 %, Sigma-Aldrich) was added as the ball milling media. Two different sizes of yttrium stabilized zirconia balls (Φ = 3 mm, 10 mm) were used in a weight ratio of 1 : 2.5 : 2.5 (reactant loading : 3 mm balls : 10 mm balls). The mixing of precursors was completed in a planetary ball milling machine (P-5, Fritsch) at a speed of 250 rpm for 2 hours. Afterwards, the isopropanol was removed by a rotation evaporator (BUECHI, Rotavapor R-300) at 60 °C. Then, the dried powder mixtures were calcined at 600 °C for 8 hours in alumina crucibles with a heating rate of 50 °C h^{-1}.

Subsequently, the obtained calcined intermediate LATP powders were ground manually with a mortar and pestle. To break the hard agglomerates in the powders after calcination, they were mechanically milled again by the planetary ball mill for 4 hours at a speed of 250 rpm using yttrium stabilized zirconia balls (Φ = 3 mm) with a weight ratio of 1 : 10 (calcined powders : 3 mm balls). After separation of the milling balls and materials, the powders were obtained by drying them overnight at 70 °C at10 mbar.

The stoichiometric and Li_2CO_3-excess calcined intermediate LATP powders were used to prepare solid electrolytes, respectively, according to the following press and sintering steps. Firstly, the powders were fed into a cylindrical mold with a diameter of 11 mm and pressed under a uniaxial pressure of 150 MPa. Then, the pre-shaped pellets were pressed again under isostatic pressure of 500 MPa. Subsequently, the pressed green bodies were sintered on alumina plates in a muffle furnace at different temperatures, which were varied from 800 °C to 900 °C for stoi-LATP and from 750 °C to 850 °C for exc-LATP with temperature interval of 25 °C. The heating rate was 50 °C h^{-1} with 6 hours dwell time for all the sintering processes at all the temperatures. Direct after sintering, the pellets were polished with SiC sandpaper (P2000) to remove possible impurities on the surfaces of the samples. The thicknesses of the obtained pellets were between 0.7 mm and 1.3 mm. Finally, the prepared LATP pellets were stored in an Ar-filled glove box ($H_2O \leq 0.1$ ppm, $O_2 \leq 0.1$ ppm) before any measurement to exclude the moisture influence.

2.2. Characterization of the obtained LATP solid-electrolytes

The relative densities of the sintered pellets were determined by Archimedes method using absolute ethanol as fluid media and theoretical density of 2.92 g cm^{-3} for $Li_{1.3}Al_{0.3}Ti_{1.7}(PO_4)_3$ [36]. The elemental composition of the calcined powders and the representative sintered pellets was

quantified by inductively coupled plasma optical emission spectrometry (ICP-OES, Thermo Scientific iCAP7600).

The sintering behaviors of the stoichiometric and the Li_2CO_3-excess calcined intermediate LATP powders were examined by dilatometry (NETZSCH, DIL 402 Expedis Classic) measurements. The sample preparation method for the dilatometry tests followed the same two-step pressing technique as that for the LATP green pellet preparation, except using a cuboidal pressing mold with a length of 15 mm instead of a cylindrical pressing mold. The dilatometry tests were conducted using a heating rate of 50 °C h^{-1} and a 40 hours dwell time at 850 °C.

The phase compositions of the stoichiometric and Li_2CO_3-excess calcined intermediate LATP powders and their crystal structures of the sintered pellets were measured by X-ray diffractometer (EMPYREAN, Panalytical) using the Cu Kα radiation. The X-ray diffraction (XRD) diagrams were collected in a 2θ range from 10° to 60° at 40 kV, 40 mA with a step size of 69.95 s / 0.009°. The phase contributions and lattice constant parameters of the sintered pellets were obtained by refining the XRD raw data using FullProf Suite.

The morphologies of the calcined intermediate LATP powders and the sintered pellets were analyzed by using the scanning electron microscope (SEM) (Quanta FEG 650) with backscattered electron signals (BSE). The element distributions of the sintered pellets were examined by the energy-dispersive X-ray (EDX) detector at an operating voltage of 10 kV. Water-free polishing of the sintered pellets was carried out prior to SEM imaging [16]. Transmission electron microscope (TEM) was used to characterize the grains and grain boundaries for the sintered pellets. To prepare TEM specimens, small pieces of the sintered LATP pellets were first mechanically ground (Struers, Tegramin-25) to a thickness of ~50 μm, then followed by thinning with Ar ion milling in a Bal-Tec Res-120 ion beam milling system. High resolution TEM (HR-TEM) images and EDX

chemical analysis were carried out at 200 kV with an FEI Tecnai F20 microscope equipped with an EDX detector.

The electrochemical properties of stoi-LATP and exc-LATP pellets were tested with a potentiostat (SP-200, Bio-Logic) using 20 mV amplitude at frequencies between 3 MHz and 100 Hz at 25 °C. Before the AC impedance measurements, thin gold films were sputtered on both sides of the sintered pellets as blocking electrodes. The obtained impedance data were fitted by "Z-View" (Scribner Associates). The total conductivity (σ_{tot}) can be calculated using Eq. 1.

$$\sigma_{tot} = L/A(R_g + R_{gb}) \quad \text{Eq. 1}$$

where R_g is the grain resistance, R_{gb} is the grain boundary resistance, A is the electrode area and L is the sample thickness.

To identify the bulk and grain boundary contributions separately, a high-frequency (3 GHz ~ 10 MHz) and normal-frequency (10 MHz ~ 1 Hz) impedance measurements were performed separately using a commercial electrochemical system (Novocontrol, Turnkey Broadband System Concept 80, Agilent E4991B and Alpha-A). The impedance spectra were collected in the temperatures range from -30 °C ~ 60 °C with an increment of 10 °C. The brick-layer-model was applied to calculate the specific grain and grain boundary conductivities using the following equation [37].

$$\sigma_g = L/AR_g, \quad \sigma_{gb} = L_{gb}/AR_{gb} = (L/AR_{gb})\left(C_g/C_{gb}\right) \quad \text{Eq. 2}$$

where L_{gb} is the total grain boundary thickness perpendicular to the electrodes, C_g is the grain capacitance and C_{gb} is the grain boundary capacitance. As the impedance spectrum is simulated using a constant phase element (*CPE*) rather than a real capacitor, the effective capacitance were derived from the fitting results is

$$C = CPE^{1/n}R^{(1/n-1)} \quad \text{Eq. 3}$$

where *C* is the true capacitance, *n* is the degree of non-ideality (0.7 ~ 1) and *R* is the resistance.

To test the reproducibility of the experimental data, the impedance measurements for the 875 °C sintered stoi-LATP and 775 °C sintered exc-LATP were repeated 3 times on different pellets with different thicknesses (0.7 mm ~ 1.3 mm).

3. Results and discussion

Table 1 lists the elemental compositions of the 600 °C calcined stoichiometric and Li_2CO_3-excess intermediate LATP powders, where the stoichiometry of Li, Al, and Ti is normalized to P. To investigate the stoichiometry of the sintered samples, the elemental compositions of 875 °C sintered stoi-LATP and 775 °C sintered exc-LATP are also given in Table 1. The stoichiometric calcined powders have comparable Li stoichiometry with the target composition of LATP. However, after sintering them at 875 °C for 6 hours, around 0.04 mol Li-deficiency is discovered. This reveals the necessity to add an extra Li sources to the precursor to compensate for the Li^+ loss during sintering. For the Li_2CO_3-excess calcined intermediate LATP powders, 0.16 mol Li-excess is observed after the calcination. While for 775 °C sintered exc-LATP, only 0.05 mol Li-excess is found, which means that the added 10 wt. % Li-excess is able to compensate the Li-loss during sintering. Apart from the change of Li amount before and after sintering for both samples, the other elements show good agreement with the target composition of LATP.

It needs to be mentioned that the amount of Li_2CO_3-excess is optimized to 10 wt. %. Based on our experimental results, 5 wt. % excess Li_2CO_3 was not as efficient as 10 wt. % excess Li_2CO_3 in reducing the sintering temperature of LATP. However, 15 wt. % excess Li_2CO_3 would generate a large amount of impurities, which deteriorates the electrical performance of LATP. Besides, the calcination temperature was set at a moderate value of 600 °C. Lower calcination temperature may

lead to the gas formation during sintering [38], while a too high calcination temperature may reduce the sintering activity of the calcined intermediate LATP powders [32]. Therefore, the following discussion will be focused on the 600 °C calcined stoichiometric and 10 wt. % Li_2CO_3-excess intermediate LATP powders and relevant LATP electrolytes made from these powders.

Table 1 Comparison of the stoichiometry of 600 °C calcined stoichiometric and 10 wt. % Li_2CO_3-excess intermediate LATP powders along with their 875 °C sintered stoi-LATP and 775 °C sintered exc-LATP pellets with targeted LATP ($Li_{1.3}Al_{0.3}Ti_{1.7}(PO_4)_3$).

	Li (mol)	**Al (mol)**	**Ti (mol)**	**P (mol)**
targeted LATP	1.3	0.3	1.7	3
stoichiometric powders	1.32 ± 0.02	0.30 ± 0.01	1.65 ± 0.04	3
10 wt. % Li_2CO_3-excess powders	1.46 ± 0.03	0.30 ± 0.02	1.69 ± 0.03	3
875 °C sintered stoi-LATP	1.26 ± 0.04	0.29 ± 0.01	1.68 ± 0.06	3
775 °C sintered exc-LATP	1.35 ± 0.06	0.30 ± 0.02	1.71 ± 0.02	3

3.1. Morphological and chemical features of the calcined precursor powders

The morphological and chemical features of the calcined intermediate LATP powders have a significant influence on the sintering behavior of LATP. To improve the homogeneity and promote the sintering activity of the powders, a mechanical ball milling step was added before the sintering step. Figure 1 shows the SEM images of both calcined powders with and without mechanical milling. As can be seen in Figure 1a and 1d, before mechanical milling, both calcined powders as obtained are severely agglomerated. It is reported by Hu *et al*. that the calcined LATP powders tend to form big agglomerates when $NH_4H_2PO_4$ is used as the $(PO_4)^{3-}$ source for the synthesis [39]. In contrast, both of the calcined powders that are mechanically milled for 4 hours exhibit homogeneous particle sizes below 1.5 μm (cf. Figure 1b and 1e) due to the fact that mechanical milling effectively shatters the hard agglomerates [40]. As shown in Figure 1c and 1f, the particle sizes of both samples are quite similar. The particles characterized by enlarged surface areas

compared with that in the samples without mechanical milling. In general, a larger specific surface area leads to a higher rate of material transport and faster densification during sintering as the driving force for the sintering process is the reduction in surface energy [41]. The same is true of the improved sintering activities of the milled intermediate LATP powders (cf. Figure S1).

It needs to be noted that the calcination temperature for the precursors was 600 °C, which is below the temperature required (≥ 750 °C) to fully crystallize LATP [29]. This means the

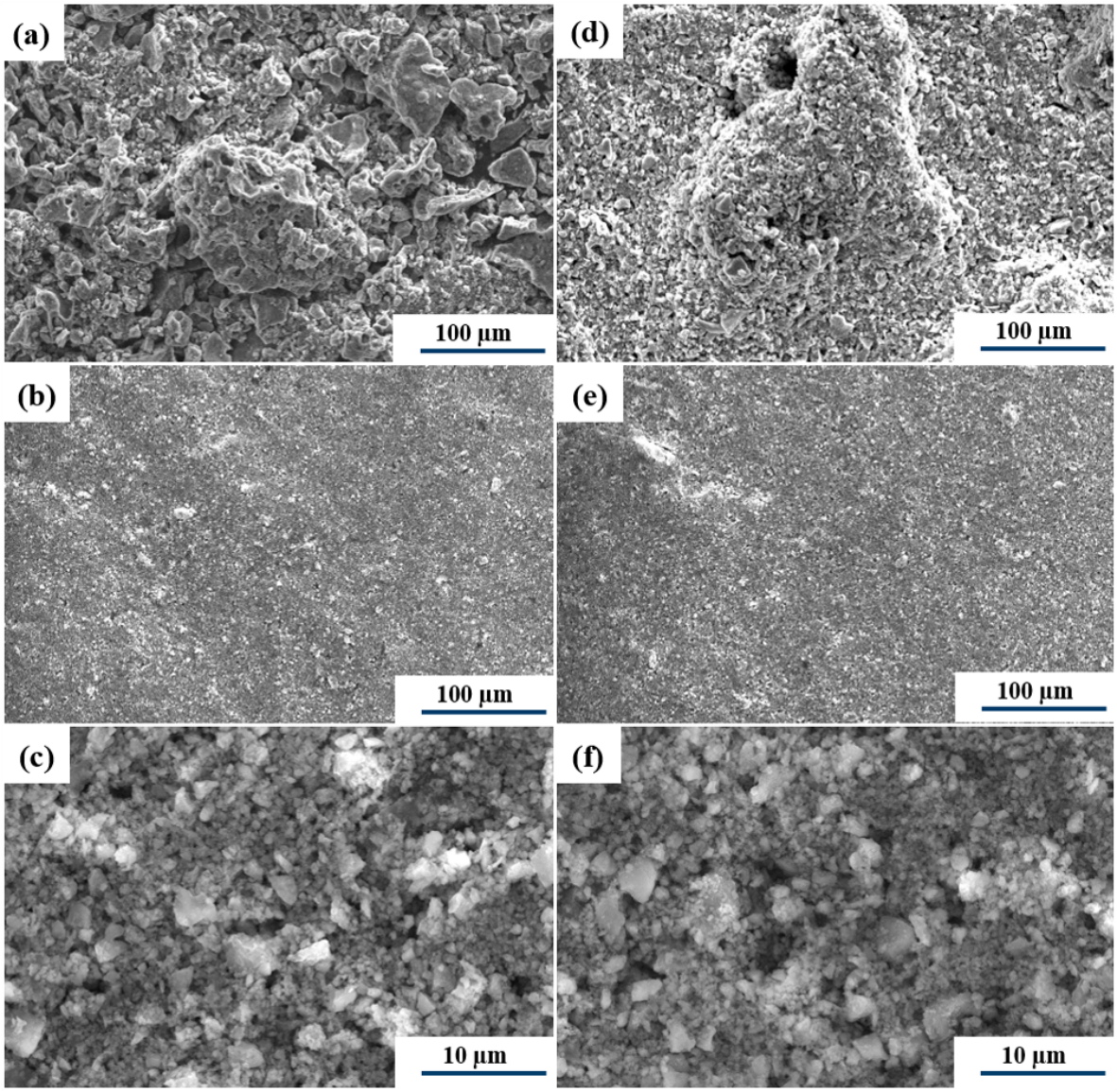

Figure 1 Stoichiometric calcined intermediate LATP powders before (a) and after (b) (c) 4 hours ball milling; 10 wt. % Li_2CO_3-excess calcined intermediate LATP powders before (d) and after (e) (f) 4 hours ball milling.

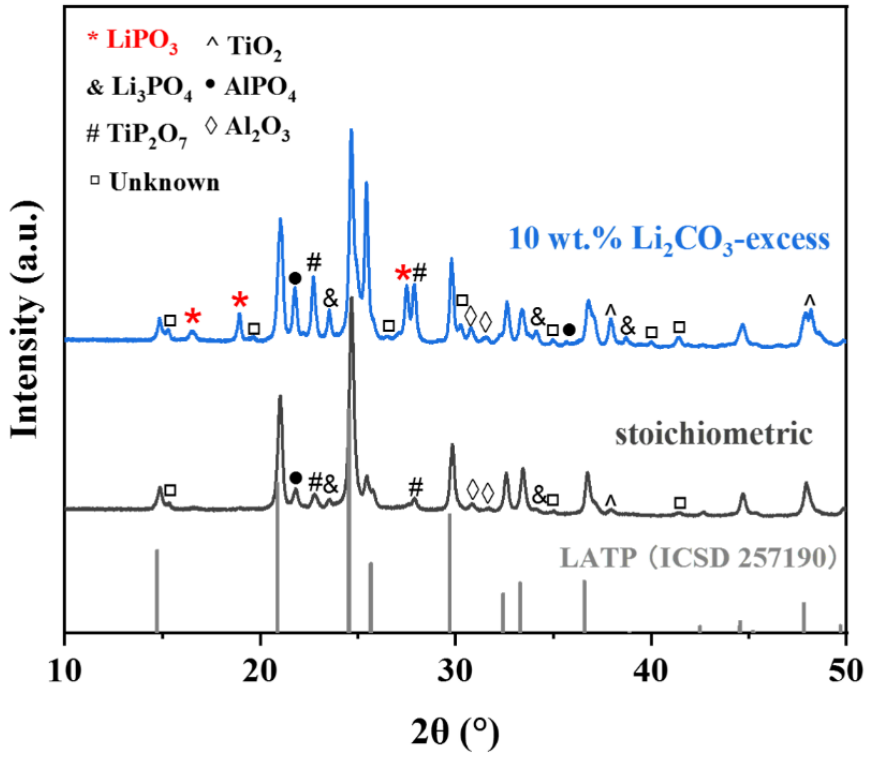

Figure 2 XRD patterns of 600 °C calcined stoichiometric and 10 wt. % Li_2CO_3-excess intermediate LATP powders. The standard XRD patterns are $LiPO_3$ ICSD-51630, Li_3PO_4 ICSD-10257, TiP_2O_7 ICSD-189807, TiO_2 ICSD-9852, $AlPO_4$ ICSD-97546, Al_2O_3 ICSD-82504 and $Li_{1.3}Al_{0.3}Ti_{1.7}(PO_4)_3$ ICSD-257190.

following sintering is a reactive sintering process. Therefore, in addition to the possible influence that comes from the inhomogeneity of particle size of the calcined intermediate LATP powders, the phase compositions may also play an important role in determining the reactive sintering of stoi-LATP and exc-LATP. As represented in Figure 2, both calcined powders have predominantly LATP phase, indicating that the powder mixtures have partially crystallized into LATP during the calcination step. Besides, except for the common intermediate phases of Li_3PO_4, TiP_2O_7 and Al_2O_3, the monoclinic $LiPO_3$ is exclusively present in the Li_2CO_3-excess calcined powders. Among these intermediates, $LiPO_3$ is the only one that has a melting point below 1000 °C (656 °C) [42], signifying that the liquid phase of $LiPO_3$ can be formed while the sintering of the green body made from the Li_2CO_3-excess calcined powders. In general, liquid phase sintering effectively accelerates

the densification process. Therefore, the calcined powders with Li_2CO_3-excess might be densified at a lower temperature compared to the stoichiometric calcined powders due to the existence of $LiPO_3$ liquid phase.

3.2. Sintering and structural features of stoi-LATP and exc-LATP

The shrinkages for both calcined powders during sintering are investigated by the dilatometry measurements, as the results shown in Figure 3a. The temperature dependent shrinkage speeds of both samples are shown in Figure 3b. Both samples have similar measured densities for their green pellets at around 2.12 g cm^{-3}. After the thermal cycle, the measured densities of stoi-LATP and exc-LATP have reached 2.73 g cm^{-3} and 2.75 g cm^{-3}, respectively. As shown in Figure 3a and 3b, the onset of sintering starts from ~550 °C for both samples. The initial slow shrinkage at temperatures around 630 °C is attributed to the rearrangement of particles and the chemical reactions between the intermediate phases to form LATP (cf. Figure 3b) [43]. As the theoretical density of LATP is in the middle among the intermediate phases (theoretical densities: TiO_2 > Al_2O_3 > TiP_2O_7 > LATP > $AlPO_4$ > $LiPO_3$ > Li_3PO_4), the specimens could contract or expand depending on the volume changes of specific chemical reactions. Besides, it is observed that the initial shrinkage process of exc-LATP happens at a slightly higher temperature than that for stoi-LATP, indicating that the crystallization of LATP made from exc-LATP starts at higher temperature compared with that from stoi-LATP which might be attributed to their different concentrations of intermediate phases (cf. Figure 2). At a sintering temperature of 700 °C, the XRD patterns for stoi-LATP and exc-LATP (cf. Figure S2) show that the phase composition is mainly LATP with only minor impurities, suggesting that the sintering shrinkage for both samples in the higher temperature will mainly come from sintering between LATP-LATP particles. When the temperature is higher than 700 °C, both samples come into their fast sintering shrinkage stages.

As demonstrated in Figure 3b, a closer inspection of the diagram reveals that stoi-LATP has only one broad shrinkage peak. In contrast, two distinct sharper shrinkage peaks are observed for exc-LATP. One shrinkage peak at 708 °C for exc-LATP is attributed to the liquid phase sintering behavior due to the existence of the intermediate product $LiPO_3$. It needs to be clarified that the

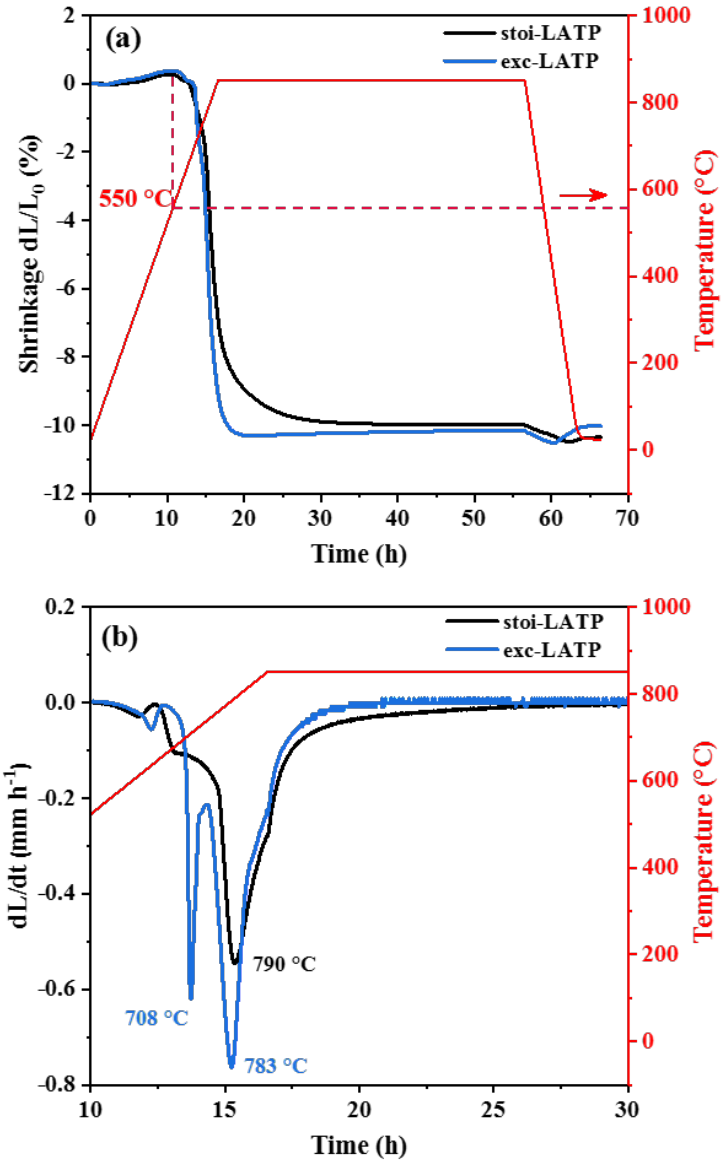

Figure 3 (a) Dilatometry measurement: shrinkages in the length direction of stoi-LATP and exc-LATP. And (b) shrinkage rates of stoi-LATP and exc-LATP according to the dilatometry curves in (a).

Li_2CO_3-excess calcined powders contain both Li_3PO_4 and $LiPO_3$ intermediate phases. If these two intermediates evolve into a solid solution, the melting temperature of each composed intermediate phase would be changed. From the Li_3PO_4-$LiPO_3$ binary phase diagram, the melting temperature of $LiPO_3$ increases with increasing Li_3PO_4 concentration in the system [42]. Therefore, the shrinkage peak temperature for exc-LATP at 708 °C is higher than the melting point of pure $LiPO_3$ (656 °C). Besides, it also reveals that the extra Li_2CO_3 does not directly act on the sintering process of LATP but rather the produced intermediated phase Li_3PO_4-$LiPO_3$ after calcination, which facilitates the liquid phase sintering behavior of exc-LATP. Another shrinkage peak temperature for exc-LATP is observed at a similar temperature (783 °C) compared with 790 °C for stoi-LATP. There are two possible reasons for exc-LATP to possess a higher shrinkage rate at 783 °C. Firstly, due to excessive amount of Li_2CO_3 precursor, exc-LATP might contain some Li-rich glassy phases which can act as sintering additives [20,35] (cf. Figure 3b) and accelerate the sintering speed. Secondly, exc-LATP might have a favorable microstructure for a faster mass transport because densification process is related to the differences in pressure and concentration gradients due to differences in radius of curvatures between convex particle surfaces and concave grain boundary necks [44].

During cooling, stoi-LATP and exc-LATP showed different contraction and/or expansion behaviors. As displayed in Figure 3a, after 56 hours, the shrinkages of both samples are referred to the cooling contraction. The cooling contraction for exc-LATP stops at about 60 hours. Afterwards, exc-LATP starts to have a minor expansion. Whereas, after 60 hours, stoi-LATP has no obvious expansion. It is known that NASICON-type materials have the intrinsic property of a thermal expansion anisotropy [45]. Therefore, during cooling, the over-sintered LATP which consists of coarser grains tends to accumulate stress and as a consequence, cracks are generated.

The crack formation can be macro-expressed as the expansion of the sample. Hence, after 60 hours, at around 400 °C, exc-LATP expands even though it is a cooling process. This suggests that the optimum sintering temperature of exc-LATP is lower than 850 °C. While, to fully densify stoi-LATP, the sintering temperature should be higher than 850 °C. Overall, the dilatometry test clearly suggests that 10 wt. % Li_2CO_3-excess can improve the sintering activity and shorten the sintering time of LATP ceramic.

To investigate the crystal structure and phase purity of the as-obtained LATP solid electrolytes, XRD measurement is carried out for stoi-LATP and exc-LATP pellets sintered at different temperatures. As is shown in Figure 4, the main reflexes are assigned to rhombohedral symmetry space group R - 3c h that indexed to the standard $Li_{1.3}Al_{0.3}Ti_{1.7}(PO_4)_3$ pattern. According to the Rietveld refinement results (cf. Figure S3 and S4) of each sample, the lattice constants and phase contributions are listed in Table 2. The lattice constants obtained from the XRD patterns of stoi-LATPs and exc-LATPs are in agreement with previous publications [15, 45] which have the same theoretical Al substitution level ($Li_{1+x}Al_xTi_{2-x}(PO_4)_3$, x = 0.3) as that of this work. In the selected sintering temperature range, the obtained stoi-LATP pellets have no detectable impurity phase, implying that sintering of LATP below 1000 °C prevents the formation of secondary phases like $AlPO_4$ and TiO_2 [17,46,47]. For exc-LATPs, except for the predominant LATP phase, a minor $LiTiOPO_4$ secondary phase is discovered at all sintering temperatures. The formation of $LiTiOPO_4$ secondary phase in exc-LATPs is in accordance with previous publications, which also employ excessive amount of Li-salts for the synthesis of LATP [35, 49]. Moreover, the obtained lattice constants for exc-LATPs and stoi-LATPs are comparable despite that a certain amount of Ti is consumed to form $LiTiOPO_4$ secondary phase for exc-LATPs. As known that apart from some crystallized impurities, the grain boundary of LATP is in an amorphous state. Hence, the measured

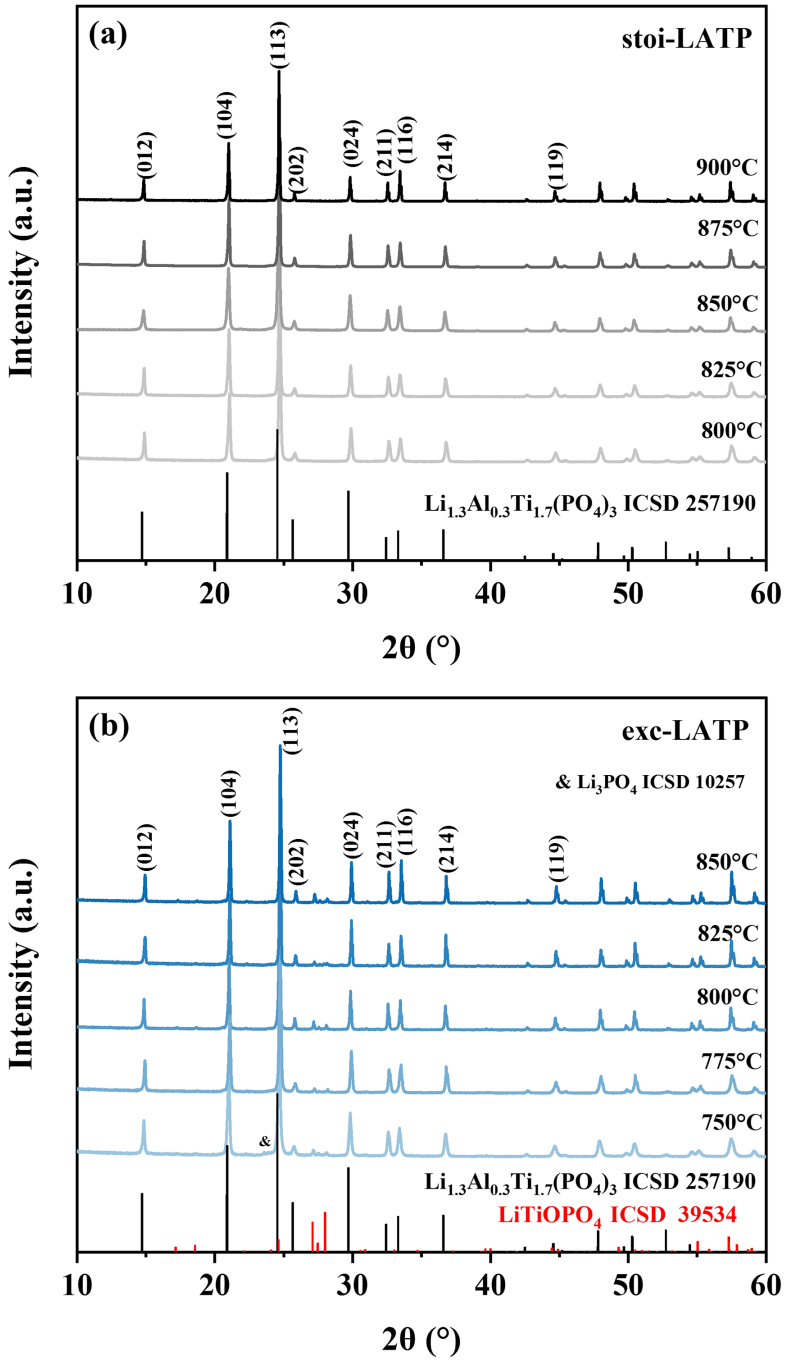

Figure 4 XRD patterns of different temperatures sintered (a) stoi-LATP and (b) exc-LATP pellets.

XRD data mainly describes the grain properties of LATP. Besides, it is indicated in Table 2 that the amount of $LiTiOPO_4$ secondary phase increases with increasing the sintering temperatures, in which 6.66 int. % of the total integrated intensities is taken by the $LiTiOPO_4$ for exc-LATP sintered

at 750 °C and 10.07 int. % for the one sintered at 850 °C. In addition to $LiTiOPO_4$, a tiny amount of Li_3PO_4 impurity is observed in the 750 °C sintered exc-LATP. For both stoi-LATP and exc-LATP, the unit cell volumes become smaller as increasing the sintering temperatures (cf. Table 2), indicating an enhancement in their crystallinity and compositional homogeneity [48]. Additionally, it should be noted that the $LiPO_3$ observed in the 600 °C calcined Li_2CO_3-excess intermediate LATP powders is no more detectable after sintering, which suggests that $LiPO_3$ is only an intermediated product, which reacts with other intermediate phases during the sintering step and forms either LATP or impurities (e.g. $LiTiOPO_4$).

Table 2 The refined lattice parameters and secondary phase fractions for different temperatures sintered stoi-LATP and exc-LATP.

Temperature (°C)	**stoi-LATP**			**exc-LATP**			
	a (Å)	**c (Å)**	**V (Å^3)**	**a (Å)**	**c (Å)**	**V (Å^3)**	**$LiTiOPO_4$ (int. %)**
750				8.503(8)	20.807(4)	1302.8(0)	6.66
775				8.501(1)	20.814(3)	1302.6(4)	7.23
800	8.502(2)	20.804(1)	1302.4(1)	8.502(7)	20.805(8)	1302.5(7)	7.71
825	8.501(9)	20.806(4)	1302.4(6)	8.503(0)	20.801(3)	1302.5(8)	9.03
850	8.498(9)	20.811(0)	1301.8(2)	8.499(0)	20.791(6)	1301.8(5)	10.07
875	8.501(8)	20.800(3)	1301.8(3)				
900	8.500(4)	20.798(1)	1301.4(9)				

The optimum sintering temperatures for stoi-LATP and exc-LATP are identified by calculating the relative densities of the sintered pellets. Since the $LiTiOPO_4$ secondary phase in exc-LATP has a higher theoretical density (3.23 g cm^{-3}) than that of LATP (2.92 g cm^{-3}), the relative densities of exc-LATP samples are calculated based on the Rietveld refinement results (cf. Table 2). As demonstrated in Figure 5, the relative densities for both stoi-LATP and exc-LATP are correlated to the sintering temperatures and showed the same trend that first increased due to densification, and subsequently slightly dropped. The decline of relative densities at higher

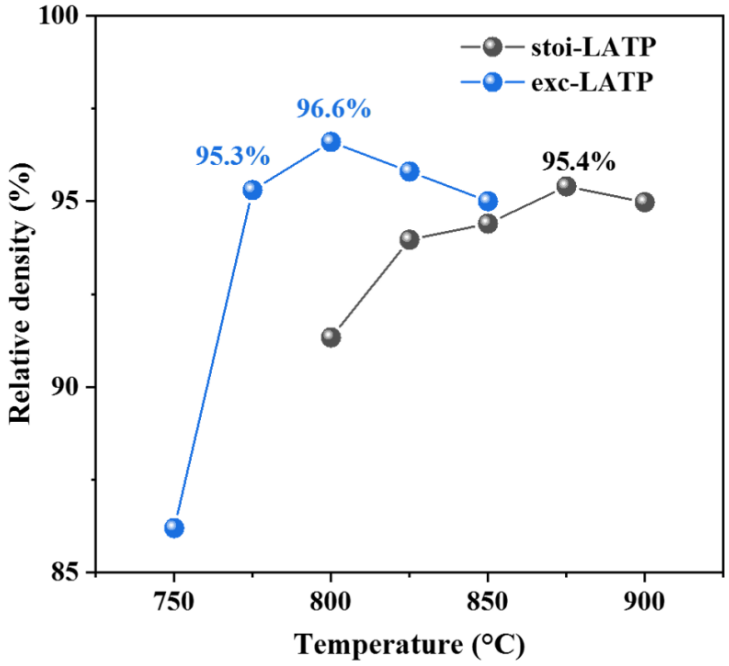

Figure 5 Relative density dependency on the sintering temperature of stoi-LATP and exc-LATP pellets.

sintering temperatures is attributed to the formation of microcracks due to over-sintering as having been explained by Dashjav *et al.* [45]. Stoi-LATP can reach the highest value of 95.4 % of its theoretical density at the sintering temperature of 875 °C, while comparable relative density can be reached at 775 °C for exc-LATP. Moreover, a higher relative density of 96.6 % is achieved for exc-LATP at 800 °C. The result confirms that 100 °C lower sintering temperature is sufficient for the LATP samples prepared with 10 wt. % Li_2CO_3-excess.

The variation of sample relative densities upon different sintering temperatures is also evidenced by their changes in microstructures. Figure 6 shows the microstructures of stoi-LATP and exc-LATP sintered at different temperatures. For stoi-LATP sintered at 800 °C in Figure 6a, as a consequence of insufficient sintering, its microstructure is characterized by a small grain size (~0.5 μm) with many voids between the grains. When the sintering temperature of stoi-LATP

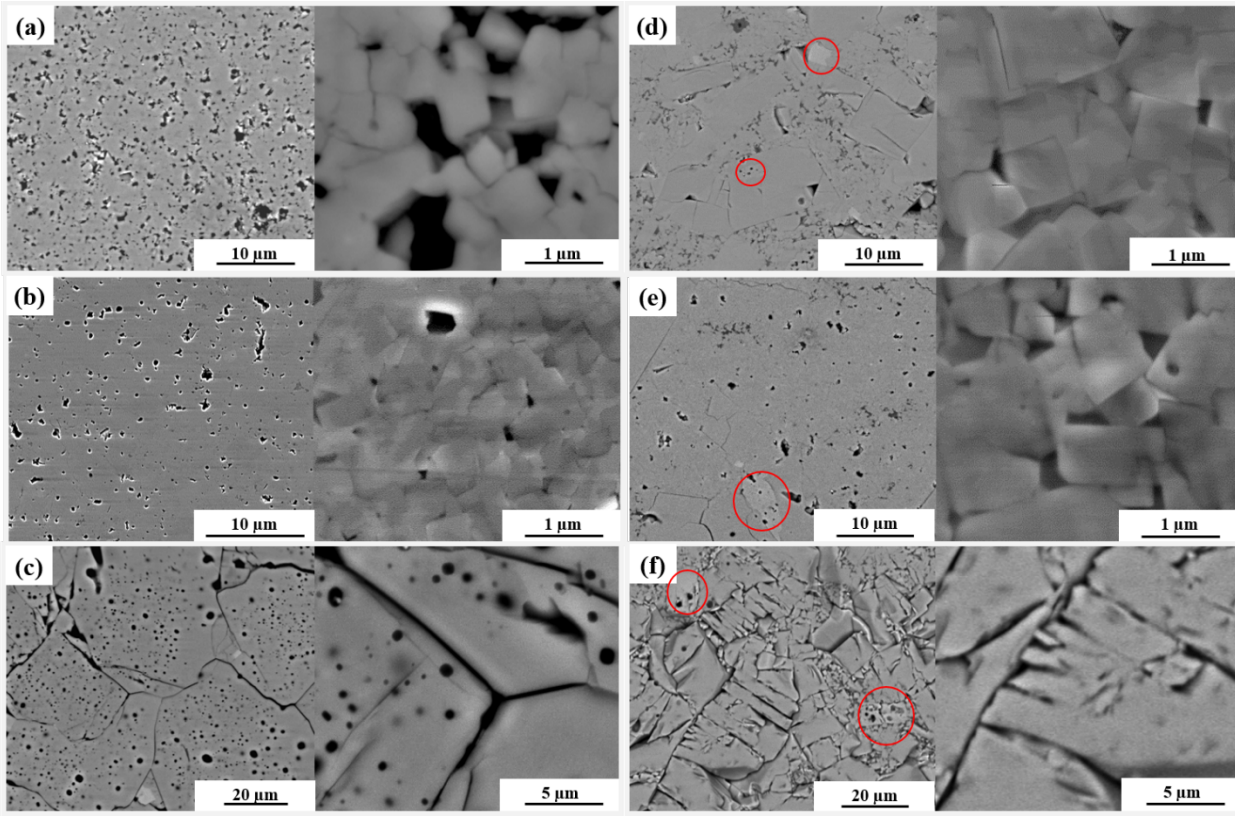

Figure 6 SEM micrographs (BSE) of stoi-LATP sintered at (a) 800 °C, (b) 875 °C, (c) 900 °C and exc-LATP sintered at (d) 775 °C, (e) 800 °C, (f) 850 °C. The particles that highlighted in red circles are $LiTiOPO_4$. The high magnification micrograph of each sample is randomly imaged within the same sample, except for (d) and (e) are selectively chosen to image the fine-grain areas.

increased to 875 °C (cf. Figure 6b), despite the grain size remains the same, the sample becomes more compact. This suggests that by increasing the sintering temperature of stoi-LATP from 800 °C to 875 °C, the densification degree of the sample is improved without significant grain growth. However, as shown in Figure 6c, further increasing in the sintering temperature of stoi-LATP, even by only 25 °C, to 900 °C, a microstructure with extraordinary huge grains (~25 µm) and severe intergranular cracks and intragranular pores is displayed. The formation of cracks for the 900 °C sintered stoi-LATP is mainly ascribed to the anisotropy of the thermal expansion during cooling process [50]. Jackman *et al.* observed that these cracks are triggered when the grain size of LATP exceeds a critical value of 1.6 µm [51]. Hence, the low relative density of stoi-LATP

sintered at 900 °C is attributed to the large amount of cracks and intergranular pores that are formed by over-sintering.

Expressively different microstructures are found for exc-LATP compared with that for stoi-LATP. When sintering exc-LATP at 775 °C and 800 °C (cf. Figure 6d and 6e), the LATP grains are highly compacted with similar grain size in the fine-grain areas. Further increasing the sintering temperature of exc-LATP to 850 °C, coarsening of grains and cracks along grain boundaries can be discovered (cf. Figure 6f), suggesting an over-sintering effect of this sample. In addition, unlike stoi-LATP samples which have a relatively uniform grain size distribution, a few large grains surrounded by fine grains (cf. Figure 6d-f) are observed in exc-LATP samples. The inhomogeneous grain growth behavior for exc-LATP can be attributed to the existence of low melting point liquid phase Li_3PO_4-$LiPO_3$ during sintering, which promotes grain growth locally in the areas where the liquid phase is present [52]. Similar microstructure has been reported by Davaasuren *et al.* for the LATP ceramic using 0.5 wt. % $Li_2B_4O_7$ as liquid phase sintering additive [48]. Besides, when comparing with the 875 °C sintered stoi-LATP (cf. Figure 6b), the LATP grains of 775 °C sintered exc-LATP (cf. Figure 6d) are more compact even through the sintering temperature is 100 °C lower. This indicates that the liquid phase in exc-LATP could act as a "binding agent", which tightly bonds the LATP grains by capillary force. Moreover, in both the large-grain and fine-grain areas for 775 °C sintered exc-LATP (cf. Figure 6d), the grain size is notably larger compared with stoi-LATP sintered at 875 °C (cf. in Figure 6b), indicating that 775 °C sintered exc-LATP should have a larger average grain size than that for 875 °C sintered stoi-LATP. For polycrystalline ceramics with a fixed geometry, a larger average grain size means a reduced total grain boundary area if we assume the average grain boundary thicknesses are similar for the two samples. In addition, the chemical compositions of the obtained stoi-LATP and

exc-LATP are also identified by SEM-EDX (cf. Figure S5). As discussed in the supplementary material, the brighter particles shown in Figure 6d - f are assigned to $LiTiOPO_4$ secondary phase. It is reported that $LiTiOPO_4$ has much lower Li^+ conductivity compared with that of LATP [53]. As displayed in Figure 6d and 6e, the $LiTiOPO_4$ particles are tightly surrounded by LATP particles and isolated distributed in the LATP matrix. Hence, we assume that the $LiTiOPO_4$ secondary phase could increase minor tortuosity for Li^+ diffusion within the sample which would have only minor influence on the overall ionic conductivity of exc-LATPs. It is acknowledged that the grain boundaries in LATP have a much lower conductivity compared with that for LATP grains [16]. Hence, the microstructures for exc-LATP samples should be more favorable for improving the total ionic conductivity.

3.3. Correlation of Li^+ transportation and microstructure

Ionic conductivities of the as-obtained LATP electrolytes are one of the most important properties which determine their feasibilities in all-solid-state batteries. Figure 7a and 7b show the experimental and fitted Nyquist plots measured between 3 MHz and 100 Hz at 25 °C for stoi-LATP pellets and exc-LATP pellets sintered at different temperatures, respectively. Ideally, the Nyquist plot of LATP should compose of two semicircles where the high-frequency semicircle represents the grain response and the middle-frequency semicircle represents the grain boundary response [16]. However, due to the extremely low RC time constant of LATP grains at room temperature, the grain impedance correlated semicircle cannot be detected in the used frequency range [7,54]. Thereby, as represented in Figure 7a and 7b, each Nyquist plot only composes of one semicircle, which is related to the grain boundary impedance, and an inclined spike, which is attributed to the Warburg-type impedance due to the Li-blocking electrodes (Au). Therefore, migration of Li^+ within LATP can be described by using a resistor ($R_1 \approx$ grain resistance) in series

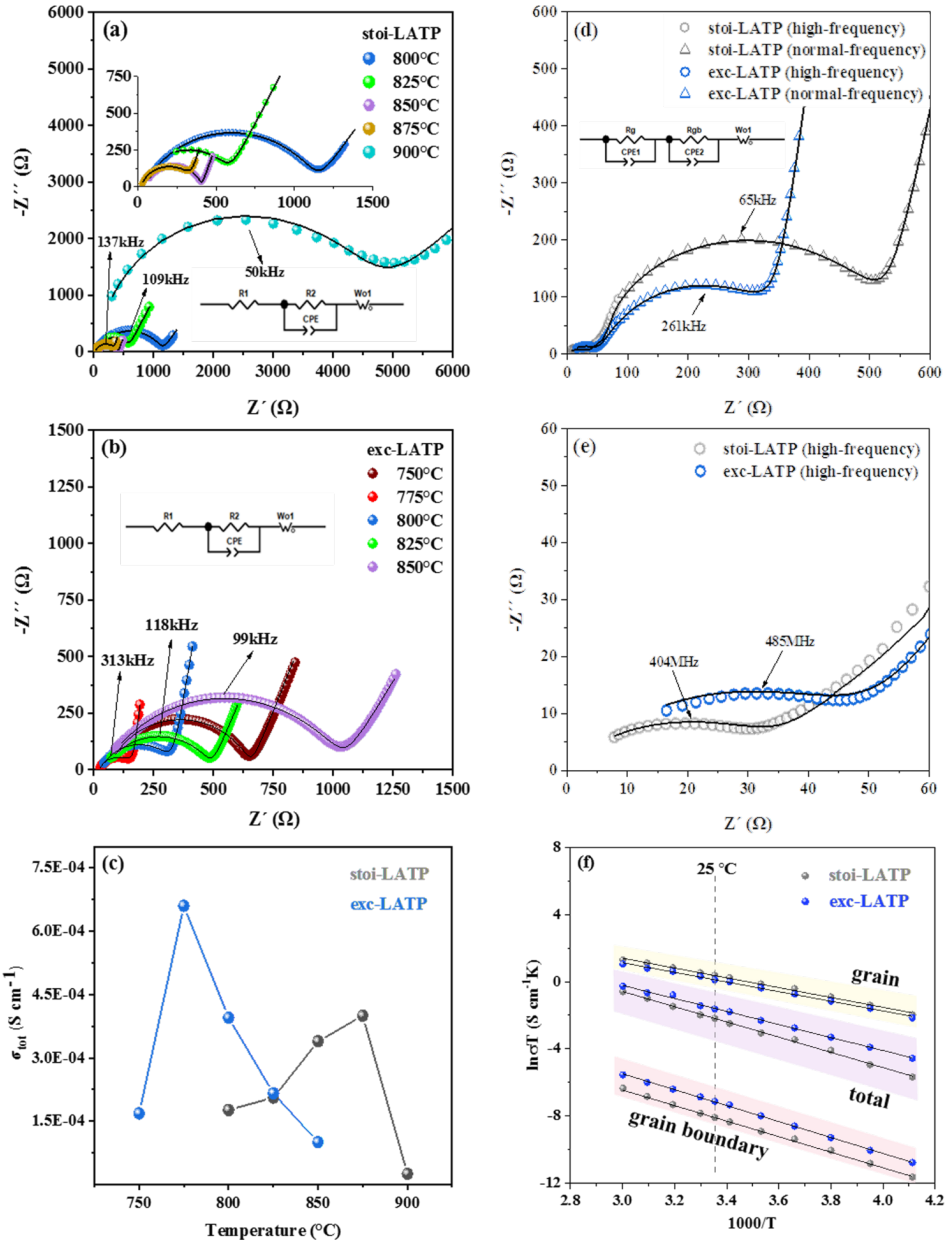

Figure 7 Nyquist plots measured at 25 °C in the frequency range of 3 MHz ~ 100 Hz for (a) stoi-LATP and (b) exc-LATP. (Measured data and fitted results are presented by symbols and solid lines, respectively.); (c) calculated total conductivities of stoi-LATP and exc-LATP sintered at different temperatures. (d) Nyquist plots measured at 25 °C in the frequency range of 3 GHz ~ 10 MHz and 10 MHz ~ 1 Hz for 875 °C sintered stoi-LATP (d: 9.37 mm, L: 1.25 mm) and 775 °C sintered exc-LATP (d: 9.23 mm, L: 1.29 mm); (e) the enlarged area for the high-frequency part; and (f) Arrhenius plots of σ_g, σ_{gb} and σ_{tot} for 875 °C sintered stoi-LATP and 775 °C sintered exc-LATP.

with an RC circuit (R_2 ≈ grain boundary resistance, *CPE*: constant phase element) and a Warburg element (W_{o1}: blocking electrode) in an equivalent circuit model, which has been inserted to

Figure 7a and 7b. Conventionally, R_1 and R_2 represent for grain and grain boundary resistance, respectively [55]. However, the precise values of these resistances can be obtained only when their correlated semicircles are visible in Nyquist plots. Hence, to avoid getting wrong conclusions, only the total conductivities are calculated based on the sum of R_1 and R_2. The total conductivities of stoi-LATP and exc-LATP pellets sintered at different temperatures are calculated based on the fitted results, as shown in Figure 7c. Since NASICON-type materials have negligible electronic conductivity (~10^{-7} mS cm^{-1}), the calculated total conductivity for each sample can be attributed to the motion of Li^+ [56]. For both stoi-LATP and exc-LATP, with increasing the sintering temperatures up to 875 °C and 775 °C, respectively, the total resistances first become smaller when higher densification of the samples are reached (cf. Figure 7a and 7b). Further increasing the sintering temperature to 900 °C and 800 °C for stoi-LATP and exc-LATP, respectively, the total resistances become larger due to cracks formation as a result of over-sintering. 875 °C sintered stoi-LATP has the smallest total resistance. Whereas, for exc-LATP, the smallest total resistance is already obtained at a sintering temperature of 775 °C. It should be mentioned that 800 °C sintered exc-LATP has a higher total resistance than that for 775 °C sintered exc-LATP even though it has the highest densification (96.6 %) (cf. Figure 5). The reason might be that 800 °C sintered exc-LATP contains more microcracks along grain boundaries (cf. Figure 6e). The best total conductivity of stoi-LATP is 0.40 mS cm^{-1} at 25 °C for 875 °C sintered sample, while higher total conductivity of 0.65 mS cm^{-1} at 25 °C is achieved by 775 °C sintered exc-LATP. Besides, three impedance measurements are performed, respectively, on 875 °C sintered stoi-LATPs and 775 °C sintered exc-LATPs. All samples show experimental errors below 5 % (cf. Table S1), suggesting a good reproducibility of the sample preparation and measurements. Additionally, it should be noted that the optimized sintering temperature (875 °C) of stoi-LATP is closer to the

over-sintering temperature (900 °C) when compared with that for exc-LATP (from 775 °C to 850 °C). For stoi-LATP, a drastic decrease of total ionic conductivity from 0.4 mS cm^{-1} to 0.02 mS cm^{-1} is found when its sintering temperature is only increased by 25 °C (from 875 °C to 900 °C). In contrast, increasing the sintering temperature of exc-LATP by 75 °C (from 775 °C to 850 °C), the obtained total conductivity is reduced from 0.65 mS cm^{-1} to 0.1 mS cm^{-1}, which is still 5 times higher than that of 900 °C sintered stoi-LATP. In short, the trend of changes for total conductivities is correlated with the variation of densities and microstructures, in which the conductivity is increased as a fact of densification and decreased as a result of cracks and/or secondary phase formation. In this work, without introducing complex chemicals or processes, Li_2CO_3 is used as both the synthesizing precursor and the sintering additive. As a consequence, the as-synthesized exc-LATP by conventional pressure-less sintering process at a relatively low sintering temperature can achieve a high density and ionic conductivity.

Since the applied 3 MHz ~ 100 Hz frequency range of impedance test is not sufficient to detect the grain response of the as-obtained LATP electrolytes, high-frequency impedance measurements are conducted for 875 °C sintered stoi-LATP and 775 °C sintered exc-LATP in order to investigate the influence of Li-excess on the specific grain and grain boundary conductivities of LATP separately. The Nyquist plots from the high-frequency (3 GHz ~ 10 MHz) and normal-frequency (10 MHz ~ 1 Hz) measurements at 25 °C for the two samples are combined and displayed in Figure 7d. Besides, to make a clear comparison between the grain conductivities for stoi-LATP and exc-LATP, the enlarged area in the high-frequency range, as is represented in Figure 7e, clearly shows the grain semicircles for the two samples. Hence, the data are fitted using two series RC circuits where the RC circuits at high- and middle-frequencies are corresponded to the grain and grain boundary responses, respectively. The fitting and calculative results according to Eq. 1,

Eq. 2 and Eq. 3 for the two samples are listed in Table 3. The obtained values of C_g and C_{gb} fit well with the characteristic capacitance for grain and grain boundary for both samples, indicating R_g = grain resistance and R_{gb} = grain boundary resistance [57]. For both stoi-LATP and exc-LATP, the grain resistances are about one order of magnitude lower than their respective grain boundary resistances. The grain conductivities of stoi-LATP and exc-LATP measured at 25 °C are 4.89 mS cm^{-1} and 3.73 mS cm^{-1} (cf. Table 3), respectively, that agree well with previous reports [15,17]. Previous studies on $Li_{1+x}Al_xTi_{2-x}(PO_4)_3$ ($0 \leq x \leq 0.5$) single crystals has revealed that the grain conductivity of LATP is determined by the number of mobile Li^+, which depends greatly on the substitution degree of Ti^{4+} by Al^{3+} [15]. Davaasuren *et al.* reported that the sintering temperature of $Li_{1.5}Al_{0.5}Ti_{1.5}(PO_4)_3$ ($Li_{1+x}Al_xTi_{2-x}(PO_4)_3$) has an influence on its composition homogeneity by comparing the unit cell volumes of LATP sintered at different temperatures [48]. The smallest unit cell volume (1296.0 $Å^3$) is obtained with the highest possible substitution degree (x = 0.5) at the sintering temperature of 900 °C. However, at the sintering temperature of 750 °C, the unit cell volume is much larger (1298.7 $Å^3$) because of a lower level of substitution (x = 0.4) due to the non-homogeneity of composition [48]. As is verified by the XRD refinement results (cf. Table 2), the unit cell volume of 775 °C sintered exc-LATP (1302.6 $Å^3$) is a bit larger than that of 875 °C sintered stoi-LATP (1301.8 $Å^3$), suggesting that exc-LATP has a lower substitution degree of Ti^{4+} by Al^{3+}. Hence, the reason for the improved grain conductivity of stoi-LATP compared with that for stoi-LATP is probably due to its higher concentration of mobile Li^+ in the grains.

For LATP, the low conductivities in the grain boundaries usually limit their improvement of total ionic conductivities [23]. The specific grain boundary conductivities of stoi-LATP and exc-LATP are calculated using Eq. 2 with taking into account of the total grain boundary thicknesses.

In grain boundary regions of LATP, some amorphous or highly disordered phases or less-conducting impurity phases exist [58]. Hence, as listed in Table 3, the specific grain boundary conductivities for both samples are about 3 orders of magnitude lower than their grain conductivities, in which 775 °C sintered exc-LATP has higher specific grain boundary conductivity (2.68×10^{-3} mS cm^{-1}) than that for 875 °C sintered stoi-LATP (1.03×10^{-3} mS cm^{-1}). Furthermore, the remarkably smaller total grain boundary resistance of 243.60 Ω is obtained for 775 °C sintered exc-LATP than for 875 °C sintered stoi-LATP (452.08 Ω). As a consequence, the total conductivity of exc-LATP achieves 0.65 mS cm^{-1} at 25 °C which is almost two times higher than that for stoi-LATP (0.38 mS cm^{-1} at 25 °C).

Table 3 Grain resistance and capacitance, grain boundary resistance and capacitance, and calculated specific grain/grain boundary and total conductivities for 875 °C sintered stoi-LATP and 775 °C sintered exc-LATP (25 °C).

	875 °C sintered stoi-LATP	**775 °C sintered exc-LATP**
R_g (Ω)	37.07 ± 0.13	51.64 ± 0.27
C_g (F)	$(7.08 \pm 0.46) \times 10^{-12}$	$(6.27 \pm 0.50) \times 10^{-12}$
R_{gb} (Ω)	452.08 ± 2.55	243.60 ± 1.58
C_{gb} (F)	$(2.76 \pm 0.07) \times 10^{-9}$	$(1.85 \pm 0.12) \times 10^{-9}$
σ_g (mS cm^{-1})	4.89 ± 0.02	3.73 ± 0.03
σ_{gb} (mS cm^{-1})	$(1.03 \pm 0.07) \times 10^{-3}$	$(2.68 \pm 0.07) \times 10^{-3}$
σ_{tot} (mS cm^{-1})	0.38 ± 0.003	0.65 ± 0.004

On the basis of the conductivities for grain and specific grain boundary as well as their total conductivities at temperatures between – 30 °C and 60 °C, activation energies of 875 °C sintered stoi-LATP and 775 °C sintered exc-LATP are calculated.

$$\sigma T = A \cdot exp\,(-E_a/kT) \qquad \text{Eq. 4}$$

where σ is the conductivity, A is the pre-exponential factor, E_a is the activation energy, k is the Boltzman constant and T is the absolute temperature. The Arrhenius plots for the two samples are drawn in Figure 7f. Table 4 lists the calculated E_a and A values from the fitted Arrhenius plots of

both samples. It can be seen that the grain activation energies are around 0.25 eV for both samples, while the grain boundary activation energies are also similar for both samples at ~0.4 eV. The higher grain boundary activation energies indicate that the major energy barrier for Li^+ migration within polycrystalline LATP comes from the grain boundaries. The total activation energy for stoi-LATP is 0.393 eV, which is in agreement with the value reported previously [59]. In contrast, despite exc-LATP has comparable grain and grain boundary activation energies as that of stoi-LATP, its total activation energy (0.331 eV) is much lower, implying that exc-LATP is energetically favorable for Li^+ conduction.

Table 4 Activation energies and pre-exponential factors (A) calculated from the Arrhenius plots in Figure 7f.

	875 °C sintered stoi-LATP		**775 °C sintered exc-LATP**	
	E_a **(eV)**	A **(S cm^{-1} K)**	E_a **(eV)**	A**(S cm^{-1} K)**
Grain	0.252 ± 0.005	26108 ± 4952	0.248 ± 0.004	17327 ± 2621
Grain boundary	0.399 ± 0.005	1686 ± 303	0.409 ± 0.004	6374 ± 969
Total	0.393 ± 0.004	255250 ± 45265	0.334 ± 0.006	89321 ± 16773

The reason for the improvement of total ionic conductivity and reduction of total activation energy for 775 °C sintered exc-LATP requires a closer examination about the relationship between the Li^+ mobility and microstructural properties. It is known that the total resistance (R_{tot}) depends on the grain resistance (R_g) and grain boundary resistance (R_{gb}).

$$R_{tot} = R_g + R_{gb} \quad \text{Eq. 5}$$

Using Eq. 1, Eq. 2 and Eq. 5, the total conductivity can be expressed as

$$\sigma_{tot} = \sigma_g \sigma_{gb} / (\sigma_{gb} + \sigma_g L_{gb}/L) \quad \text{Eq. 6}$$

As the average grain boundary thickness d_{gb} is very small compared with the average grain size d_g, the total thickness of the sample can be written as

$$L = n(d_{gb} + d_g) \approx n d_g \quad \text{Eq. 7}$$

where *n* is the number of grains that an ion passes perpendicular to the electrode. Hence, the total grain boundary thickness is depending on the average grain boundary thickness and the number of grains that an ion passes, as is given by

$$L_{gb} = nd_{gb} \approx L \cdot d_{gb}/d_g \quad \text{Eq. 8}$$

Combining the activation energies of the grain and grain boundary using Eq. 4, Eq 6 and Eq. 8, the total activation energy can be written as a function of the grain activation energy, grain boundary activation energy and the ratio of average grain and grain boundary size, as follow

$$E_{a,tot} = kTln\left[(d_{gb}/d_g)(A_{tot}/A_{gb})exp\left(-E_{a,g}/kT\right) + (A_{tot}/A_g)exp\left(-E_{a,gb}/kT\right)\right] + E_{a,g} + E_{a,gb} \quad \text{Eq. 9}$$

where $E_{a,tot}$, $E_{a,g}$ and $E_{a,gb}$ are the total activation energy, grain activation energy and grain boundary activation energy, respectively. A_{tot}, A_g and A_{gb} are the pre-exponential factors for the total, grain and grain boundary, respectively. According to the equation, the total activation energy is not only influenced by the grain and grain boundary activation energies but also depends on the ratio of average grain and grain boundary size (d_{gb}/d_g). Increasing the average grain size or reducing the average grain boundary thickness results in a smaller value of d_{gb}/d_g which is beneficial for lowing the total activation energy.

As calculated from the fitting results of the Arrhenius plots listed in Table 4, the d_{gb}/d_g values are 0.0068 and 0.0029 for the stoi-LATP and the exc-LATP, respectively. As discussed by Gunduz *et al*., despite the sintering temperatures of LATP influence the average grain size and the amount of impurities, the obtained average grain boundary thicknesses of sintered samples at different temperatures have no significant difference [60]. Accordingly, the reason for the lower d_{gb}/d_g value for the exc-LATP can be mainly attributed to its larger average grain size compared with that for the stoi-LATP, since the two samples exhibit significant different grain morphologies

as shown in Figure 6b and 6d. Moreover, the average grain boundary thicknesses of the two samples are compared and recorded by TEM in order to gain further insights into the relation of morphology and Li^+ conduction.

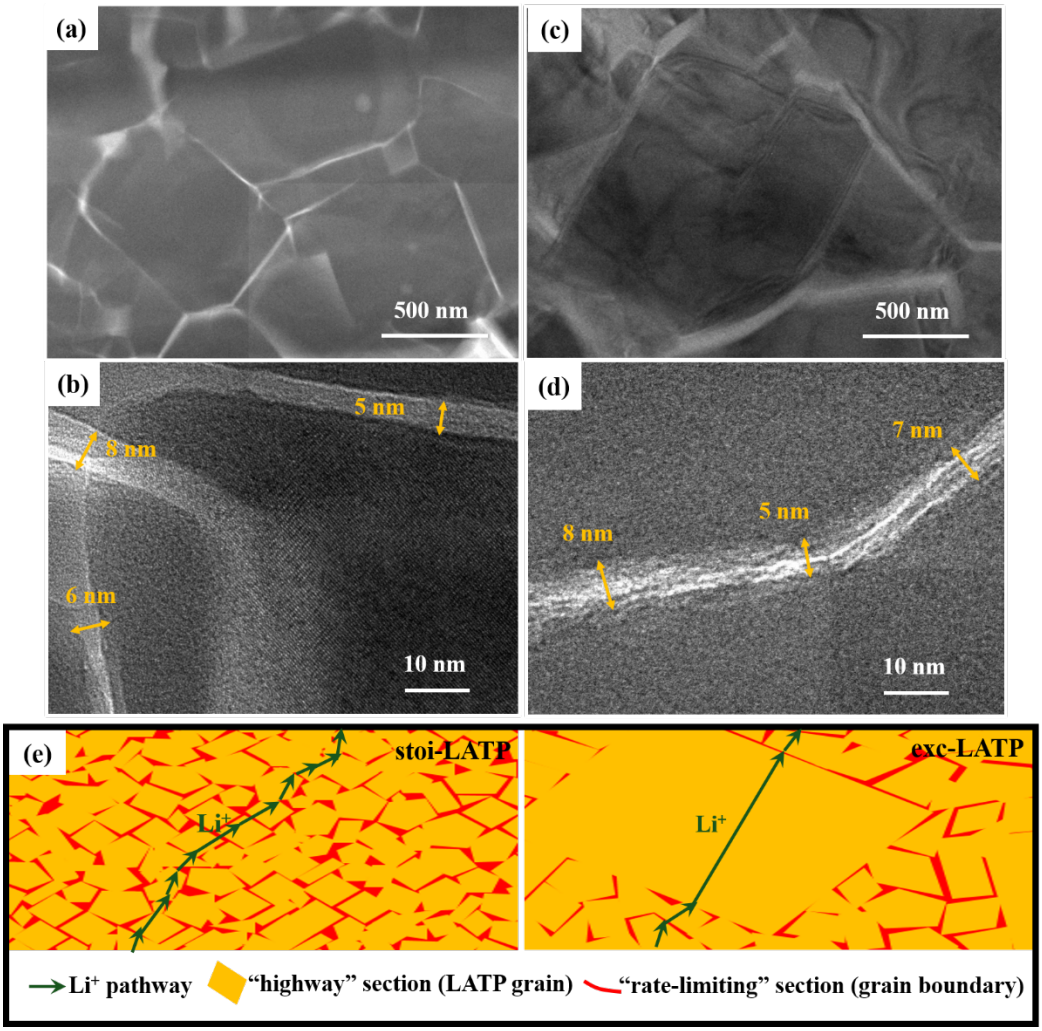

Figure 8 TEM and HR-TEM images of 875 °C sintered stoi-LATP (a, b) and 775 °C sintered exc-LATP (c, d). And schematic illustration of the transportation of Li^+ in the 875 °C sintered stoi-LATP and 775 °C sintered exc-LATP, respectively (e).

Figure 8a and 8c show the overview of TEM images of 875 °C sintered stoi-LATP and 775 °C sintered exc-LATP, respectively. The grain size of the stoi-LATP is consistent with that observed by SEM, whereas only the small grains in the exc-LATP are recorded due to the limiting focusing length of TEM. Several grain boundaries of each sample are randomly selected and measured as

the HR-TEM images are shown in Figure 8b, 8d and Figure S6. As represented in the images, the grain boundary thicknesses of the stoi-LATP and the exc-LATP are in the same range of 5 ~ 10 nm despite their sintering temperature and grain size differences. The obtained grain boundary thicknesses are in agreement with that observed previously in Ohara LATP sheets [61]. Hence, on the basis of the experimental results and previous work [60, 61], it can be concluded that the average grain boundary thickness for the two LATP samples are similar. Besides, as mentioned above, 775 °C sintered exc-LATP shows a much larger average grain size than that of 875 °C sintered stoi-LATP. Under these conditions, according to Eq. 6 and Eq. 9, the higher total ionic conductivity and lower total activation energy of the exc-LATP can be attributed to its smaller total grain boundary thickness compared with that of the stoi-LATP because of the reduced number of LATP grains that perpendicular to the electrodes.

Table 5 Quantification of TEM-EDX point analysis in grains for 875 °C sintered stoi-LATP and 775 °C sintered exc-LATP expressed with Ti, Al, and P atomic percentage proportional to each other.

		C (Ti/Al)	**C (P/Ti)**	**C (P/Al)**
	Theoretical $Li_{1.3}Al_{0.3}Ti_{1.7}(PO_4)_3$	5.67	1.76	10.00
Grain	875 °C sintered stoi-LATP	5.72	1.69	9.67
	775 °C sintered exc-LATP	6.10	1.69	10.24
Grain boundary	875 °C sintered stoi-LATP	7.13	1.62	11.44
	775 °C sintered exc-LATP	4.84	1.82	8.76

Furthermore, the chemical compositions in the grains and grain boundaries are measured by TEM-EDX for the comparative study of the two samples. 3 grains and 5 grain boundaries for each sample are measured and averaged. As listed in Table 5, the obtained averaged atomic concentration of Al, Ti, P are compared. It reveals that in the grains of the stoi-LATP, the atomic percentage ratios of $C_{(Ti/Al)}$, $C_{(P/Ti)}$ and $C_{(P/Al)}$ confirm well with theoretical $Li_{1.3}Al_{0.3}Ti_{1.7}(PO_4)_3$, while the atomic ratio of $C_{(Ti/Al)}$ in the grains of the exc-LATP deviates towards Ti excess. This

suggests a lower substitution degree of Ti^{4+} by Al^{3+} in the grain regions for the exc-LATP compared with that for the stoi-LATP. The difference in Al^{3+} substitution level by the two samples is also in accordance with the observations that 875 °C sintered stoi-LATP has a slightly smaller unit cell volume (cf. Table 2) and higher grain ionic conductivity than that of 775 °C sintered exc-LATP (cf. Table 3). In the grain boundary regions, the atomic percentage ratios of $C_{(Ti/Al)}$, $C_{(P/Ti)}$ and $C_{(P/Al)}$ for both samples show a larger discrepancy compared with the theoretical values due to the composition complexity in the grain boundaries and errors caused by the small signal/noise ratio in the tiny grain boundary areas of LATP. Nevertheless, on the basis of the comparative study of the EDX results of grain boundaries in each sample, it can be concluded that 775 °C sintered exc-LATP is enriched in Al compared with that for 875 °C sintered stoi-LATP. The difference in Al concentration at the grain boundary of each sample may be the reason for their slightly different specific grain boundary conductivities.

Figure 8e schematically illustrates the transportation of Li^+ in the two samples. The grains could be regarded as "highways" because of the high speed of Li^+ transportation. While, the grain boundaries act as "rate-limiting" traffic jam sections which limit the speed of the Li^+ to cross over. For 775 °C sintered exc-LATP, the pathways of Li^+ compose less "rate-limiting" and more Li^+ conducting grain boundaries than that of 875°C sintered stoi-LATP. Therefore, the obtained higher total ionic conductivity and lower activation energy for the exc-LATP rely on its higher specific grain boundary ionic conductivity and smaller total grain boundary thickness.

4. Conclusions

The fast Li^+ conductor LATP has been successfully synthesized by solid-state-reaction process followed by reactive sintering. Lower calcination temperature (600 °C) and subsequent

mechanical milling are employed to improve the sintering activity of LATP. As a result, stoi-LATP sintered at 875 °C can achieve a high relative density of 95.4 % without significantly compromising its ionic conductivity (0.38 mS cm^{-1}, 25 °C). Furthermore, by adding 10 wt. % excess Li_2CO_3 starting materials, the sintering temperature of LATP is reduced to 775 °C along with an enhancement of ionic conductivity to 0.65 mS cm^{-1} at 25 °C. The reduction of sintering temperature of exc-LATP is based on the existence of low melting point intermediate product Li_3PO_4-$LiPO_3$ which promotes the liquid phase sintering for a fast densification rate. Compared with the specific grain/grain boundary conductivities for 875 °C sintered stoi-LATP, 775 °C sintered exc-LATP shows a slightly lower specific grain conductivity and a higher specific grain boundary conductivity. The ionic conductivity of the as-obtained LATP pellets are directly related to their morphologies. Correlative analysis between Li^+ conductivity and microstructure indicates that the improvement of total ionic conductivity for 775 °C sintered exc-LATP compared with that of 875 °C sintered stoi-LATP is attributed to its higher specific grain boundary conductivity and smaller total grain boundary thickness, as a result of combined effects of reactive sintering and liquid phase sintering. This is of practical importance in fabricating of LATP solid electrolyte and the relevant solid-state batteries.

Supplementary material

Dilatometry test of stoichiometric calcined intermediate LATP powders before and after ball milling. XRD patterns of 700 °C sintered LATP pellets. XRD refinement results of LATP pellets sintered at different temperatures. SEM images with corresponding EDX element mapping of 875 °C sintered stoi-LATP and 775 °C sintered exc-LATP. Reproducibly of the electrochemical impedance measurements. HR-TEM images for estimating the grain boundary thicknesses of the obtained LATP.

Acknowledgements

This work was financially supported by the projects of "Materials and Components to Meet High Energy Density Batteries III" of the funding program "Excellent battery" from the Bundesministerium für Bildung und Forschung (BMBF) (Project No.: 13XP0258B). S. Basak acknowledges the project 'Electroscopy' (Grant No. :892916) from the Marie Skłodowska-Curie action.

References

[1] T. Famprikis, P. Canepa, J.A. Dawson, M.S. Islam, C. Masquelier, Fundamentals of inorganic solid-state electrolytes for batteries, Nat. Mater. 18 (2019) 1278–1291. https://doi.org/10.1038/s41563-019-0431-3.

[2] D. Liu, W. Zhu, Z. Feng, A. Guerfi, A. Vijh, K. Zaghib, Recent progress in sulfide-based solid electrolytes for Li-ion batteries, Mater. Sci. Eng. B Solid-State Mater. Adv. Technol. 213 (2016) 169–176. https://doi.org/10.1016/j.mseb.2016.03.005.

[3] S. Chen, D. Xie, G. Liu, J.P. Mwizerwa, Q. Zhang, Y. Zhao, X. Xu, X. Yao, Sulfide solid electrolytes for all-solid-state lithium batteries: Structure, conductivity, stability and application, Energy Storage Mater. 14 (2018) 58–74. https://doi.org/10.1016/j.ensm.2018.02.020.

[4] W.J. Kwon, H. Kim, K.N. Jung, W. Cho, S.H. Kim, J.W. Lee, M.S. Park, Enhanced Li+ conduction in perovskite $Li_{3x}La_{2/3-x}\square_{1/3-2x}TiO_3$ solid-electrolytes via microstructural engineering, J. Mater. Chem. A. 5 (2017) 6257–6262. https://doi.org/10.1039/c7ta00196g.

[5] C.L. Tsai, S. Yu, H. Tempel, H. Kungl, R.A. Eichel, All-ceramic Li batteries based on garnet structured $Li_7La_3Zr_2O_{12}$, Mater. Technol. 35 (2020) 656–674. https://doi.org/10.1080/10667857.2020.1746539.

[6] Li, Y.; Wang, Z.; Li, C.; Cao, Y.; Guo, X. Densification and Ionic-Conduction Improvement of Lithium Garnet Solid Electrolytes by Flowing Oxygen Sintering. J. Power Sources, 248 (2014) 642–646. https://doi.org/10.1016/j.jpowsour.2013.09.140.

[7] S. Yu, A. Mertens, X. Gao, D.C. Gunduz, R. Schierholz, S. Benning, F. Hausen, J. Mertens, H. Kungl, H. Tempel, R.-A. Eichel, Influence of microstructure and $AlPO_4$ secondary-phase on the ionic conductivity of $Li_{1.3}Al_{0.3}Ti_{1.7}(PO_4)_3$ solid-state electrolyte, Funct. Mater. Lett. 9 (2016) 1650066. https://doi.org/10.1142/s1793604716500661.

[8] S. Duluard, A. Paillassa, P. Lenormand, P.L. Taberna, P. Simon, P. Rozier, F. Ansart, J. Ihlefeld, Dense on Porous Solid LATP Electrolyte System: Preparation and Conductivity Measurement, J. Am. Ceram. Soc. 100 (2017) 141–149. https://doi.org/10.1111/jace.14451.

[9] M. Sakuma, K. Suzuki, M. Hirayama, R. Kanno, Reactions at the electrode/electrolyte interface of all-solid-state lithium batteries incorporating Li-M (M = Sn, Si) alloy electrodes and sulfide-based solid electrolytes, Solid State Ionics. 285 (2016) 101–105. https://doi.org/10.1016/j.ssi.2015.07.010.

[10] Y. Zhu, X. He, Y. Mo, First principles study on electrochemical and chemical stability of

solid electrolyte-electrode interfaces in all-solid-state Li-ion batteries, J. Mater. Chem. A. 4 (2016) 3253–3266. https://doi.org/10.1039/c5ta08574h.

[11] Zhang, Y.; Meng, J.; Chen, K.; Wu, Q.; Wu, X.; Li, C. Behind the Candelabra: A Facile Flame Vapor Deposition Method for Interfacial Engineering of Garnet Electrolyte to Enable Ultralong Cycling Solid-State Li-FeF_3 Conversion Batteries. ACS Appl. Mater. Interfaces, 12 (2020) 33729–33739. https://doi.org/10.1021/acsami.0c08203.

[12] O. Guillon, C.-L. Tsai, Q. Xu, F. Tietz, Q. Ma, A Novel Sol-Gel Method for Large-Scale Production of Nanopowders: Preparation of $Li_{1.5}Al_{0.5}Ti_{1.5}(PO_4)_3$ as an Example, J. Am. Ceram. Soc. 99 (2015) 410–414. https://doi.org/10.1111/jace.13997.

[13] E. Kobayashi, L.S. Plashnitsa, T. Doi, S. Okada, J.I. Yamaki, Electrochemical properties of Li symmetric solid-state cell with NASICON-type solid electrolyte and electrodes, Electrochem. Commun. 12 (2010) 894–896. https://doi.org/10.1016/j.elecom.2010.04.014.

[14] G. Yan, S. Yu, J.F. Nonemacher, H. Tempel, H. Kungl, J. Malzbender, R.A. Eichel, M. Krüger, Influence of sintering temperature on conductivity and mechanical behavior of the solid electrolyte LATP, Ceram. Int. 45 (2019) 14697–14703. https://doi.org/10.1016/j.ceramint.2019.04.191.

[15] D. Rettenwander, A. Welzl, S. Pristat, F. Tietz, S. Taibl, G.J. Redhammer, J. Fleig, A microcontact impedance study on NASICON-type $Li_{1+x}Al_xTi_{2-x}(PO_4)_3$ ($0 \leq x \leq 0.5$) single crystals, J. Mater. Chem. A. 4 (2015) 1506–1513. https://doi.org/10.1039/c5ta08545d.

[16] A. Mertens, S. Yu, N. Schön, D.C. Gunduz, H. Tempel, R. Schierholz, F. Hausen, H. Kungl, J. Granwehr, R.-A. Eichel, Superionic bulk conductivity in $Li_{1.3}Al_{0.3}Ti_{1.7}(PO_4)_3$ solid electrolyte, Solid State Ionics. 309 (2017) 180–186. https://doi.org/10.1016/j.ssi.2017.07.023.

[17] Y. Yoon, J. Kim, C. Park, D. Shin, The relationship of structural and electrochemical properties of NASICON structure $Li_{1.3}Al_{0.3}Ti_{1.7}(PO_4)_3$ electrolytes by a sol-gel method, J. Ceram. Process. Res. 14 (2013) 563–566.

[18] J.I. Moon, H.C. Cho, J.H. Song, Synthesis and conductive properties of $Li_{1+x}Al_xTi_{2-x}(PO_4)_3$ (x = 0, 0.3, 0.5) by sol-gel method, Korean J. Mater. Res. 22 (2012) 346–351. https://doi.org/10.3740/MRSK.2012.22.7.346.

[19] K. Arbi, W. Bucheli, R. Jiménez, J. Sanz, High lithium ion conducting solid electrolytes based on NASICON $Li_{1+x}Al_xM_{2-x}(PO_4)_3$ materials (M = Ti, Ge and $0 \leq x \leq 0.5$), J. Eur. Ceram. Soc. 35 (2015) 1477–1484. https://doi.org/10.1016/j.jeurceramsoc.2014.11.023.

[20] N. Schön, D.C. Gunduz, S. Yu, H. Tempel, R. Schierholz, F. Hausen, Correlative electrochemical strain and scanning electron microscopy for local characterization of the solid state electrolyte $Li_{1.3}Al_{0.3}Ti_{1.7}(PO_4)_3$, Beilstein J. Nanotechnol. 9 (2018) 1564–1572. https://doi.org/10.3762/bjnano.9.148.

[21] F. Han, J. Yue, C. Chen, N. Zhao, X. Fan, Z. Ma, T. Gao, F. Wang, X. Guo, C. Wang,

Interphase Engineering Enabled All-Ceramic Lithium Battery, Joule. 2 (2018) 497–508. https://doi.org/10.1016/j.joule.2018.02.007.

[22] P.Y. Yen, M.L. Lee, D.H. Gregory, W.R. Liu, Optimization of sintering process on $Li_{1+x}Al_xTi_{2-x}(PO_4)_3$ solid electrolytes for all-solid-state lithium-ion batteries, Ceram. Int. 46 (2020) 20529–20536. https://doi.org/10.1016/j.ceramint.2020.05.162.

[23] R. DeWees, H. Wang, Synthesis and Properties of NaSICON-type LATP and LAGP Solid Electrolytes, ChemSusChem. 12 (2019) 3713–3725. https://doi.org/10.1002/cssc.201900725.

[24] K. Takada, Progress in solid electrolytes toward realizing solid-state lithium batteries, J. Power Sources. 394 (2018) 74–85. https://doi.org/10.1016/j.jpowsour.2018.05.003.

[25] T. Kato, R. Yoshida, K. Yamamoto, T. Hirayama, M. Motoyama, W.C. West, Y. Iriyama, Effects of sintering temperature on interfacial structure and interfacial resistance for all-solid-state rechargeable lithium batteries, J. Power Sources. 325 (2016) 584–590. https://doi.org/10.1016/j.jpowsour.2016.06.068.

[26] Y. Liu, J. Liu, Q. Sun, D. Wang, K.R. Adair, J. Liang, C. Zhang, L. Zhang, S. Lu, H. Huang, X. Song, X. Sun, Insight into the Microstructure and Ionic Conductivity of Cold Sintered NASICON Solid Electrolyte for Solid-State Batteries, ACS Appl. Mater. Interfaces. 11 (2019) 27890–27896. https://doi.org/10.1021/acsami.9b08132.

[27] H. Guo, A. Baker, J. Guo, C.A. Randall, Protocol for Ultralow-Temperature Ceramic Sintering: An Integration of Nanotechnology and the Cold Sintering Process, ACS Nano. 10 (2016) 10606–10614. https://doi.org/10.1021/acsnano.6b03800.

[28] L. Hallopeau, D. Bregiroux, G. Rousse, D. Portehault, P. Stevens, G. Toussaint, C. Laberty-Robert, Microwave-Assisted Reactive Sintering and Lithium Ion Conductivity of $Li_{1.3}Al_{0.3}Ti_{1.7}(PO_4)_3$ Solid Electrolyte. *J. Power Sources*, 378 (2018) 48–52. https://doi.org/10.1016/j.jpowsour.2017.12.021.

[29] K.G. Schell, E.C. Bucharsky, F. Lemke, M.J. Hoffmann, Effect of calcination conditions on lithium conductivity in $Li_{1.3}Ti_{1.7}Al_{0.3}(PO_4)_3$ prepared by sol-gel route, Ionics (Kiel). 23 (2017) 821–827. https://doi.org/10.1007/s11581-016-1883-y.

[30] I. Ya Guzman, Reaction Sintering and Its Practical Application, Glas. Ceram. 50 (1993) 412.

[31] L. Hallopeau, D. Bregiroux, G. Rousse, D. Portehault, P. Stevens, G. Toussaint, C. Laberty-Robert, Microwave-assisted reactive sintering and lithium ion conductivity of $Li_{1.3}Al_{0.3}Ti_{1.7}(PO_4)_3$ solid electrolyte, J. Power Sources. 378 (2018) 48–52. https://doi.org/10.1016/j.jpowsour.2017.12.021.

[32] S. He, Y. Xu, B. Zhang, X. Sun, Y. Chen, Y. Jin, Unique rhombus-like precursor for synthesis of $Li_{1.3}Al_{0.3}Ti_{1.7}(PO_4)_3$ solid electrolyte with high ionic conductivity, Chem. Eng. J. 345 (2018) 483–491. https://doi.org/10.1016/j.cej.2018.03.151.

[33] M.N. Rahaman, Kinetics and mechanisms of densification, Sinter. Adv. Mater. (2010) 33–64. https://doi.org/10.1533/9781845699949.1.33.

[34] J. Liu, T. Liu, Y. Pu, M. Guan, Z. Tang, F. Ding, Z. Xu, Y. Li, Facile synthesis of NASICON-type $Li_{1.3}Al_{0.3}Ti_{1.7}(PO_4)_3$ solid electrolyte and its application for enhanced cyclic performance in lithium ion batteries through the introduction of an artificial Li_3PO_4 SEI layer, RSC Adv. 7 (2017) 46545–46552. https://doi.org/10.1039/c7ra09335g.

[35] K. Waetzig, C. Heubner, M. Kusnezo, Reduced Sintering Temperatures of Li^+ Conductive $Li_{1.3}Al_{0.3}Ti_{1.7}(PO_4)_3$ Ceramics, Crystals. 10 (2020) 408.

[36] J. Emery, T. Šalkus, A. Abramova, M. Barré, A.F. Orliukas, NMR Investigations in $Li_{1.3}Al_{0.3}Ti_{1.7}(PO_4)_3$ Ceramics. Part I: Structural Aspect, J. Phys. Chem. C. 120 (2016) 26173–26186. https://doi.org/10.1021/acs.jpcc.6b06764.

[37] S.M. Haile, G. Staneff, K.H. Ryu, Non-stoichiometry, grain boundary transport and chemical stability of proton conducting perovskites, J. Mater. Sci. 36 (2001) 1149–1160. https://doi.org/10.1023/A:1004877708871.

[38] T. Zangina, J. Hassan, K.A. Matori, R.S. Azis, U. Ahmadu, A. See, Sintering behavior, ac conductivity and dielectric relaxation of $Li_{1.3}Ti_{1.7}Al_{0.3}(PO_4)_3$ NASICON compound, Results Phys. 6 (2016) 719–725. https://doi.org/10.1016/j.rinp.2016.10.003.

[39] X. Hu, Y. L. Chen, Z. C. Hu, Y. Li, Z. Y. Ling, All-Solid-State Supercapacitors Based on a Carbon-Filled Porous/Dense/Porous Layered Ceramic Electrolyte. *J. Electrochem. Soc.*, *165* (2018) A1269–A1274. https://doi.org/10.1149/2.0481807jes.

[40] C. Wang, Q. Sun, Y. Liu, Y. Zhao, X. Li, X. Lin, M.N. Banis, M. Li, W. Li, K.R. Adair, D. Wang, J. Liang, R. Li, L. Zhang, R. Yang, S. Lu, X. Sun, Boosting the performance of lithium batteries with solid-liquid hybrid electrolytes: Interfacial properties and effects of liquid electrolytes, Nano Energy. 48 (2018) 35–43. https://doi.org/10.1016/j.nanoen.2018.03.020.

[41] V.M. Svistunov, V.A. Strel'tsov, Initial stage of sintering powder compacts, Sov. Powder Metall. Met. Ceram. 30 (1991) 124–129. https://doi.org/10.1007/BF00797284.

[42] R.K. Osterheld, Liquidus diagram for the system lithium orthophosphate-lithium metaphosphate, J. Inorg. Nucl. Chem. 30 (1968) 3173–3175.

[43] R.K. Bordia, S.J.L. Kang, E.A. Olevsky, Current understanding and future research directions at the onset of the next century of sintering science and technology, J. Am. Ceram. Soc. 100 (2017) 2314–2352. https://doi.org/10.1111/jace.14919.

[44] C.B. Carter, M.G. Norton, Sintering and Grain Growth, Ceram. Mater. (2013) 439–456. https://doi.org/10.1007/978-1-4614-3523-5_24.

[45] E. Dashjav, Q. Ma, Q. Xu, C.L. Tsai, M. Giarola, G. Mariotto, F. Tietz, The influence of water on the electrical conductivity of aluminum-substituted lithium titanium phosphates,

Solid State Ionics. 321 (2018) 83–90. https://doi.org/10.1016/j.ssi.2018.04.010.

[46] T. Hupfer, E.C. Bucharsky, K.G. Schell, M.J. Hoffmann, Influence of the secondary phase $LiTiOPO_4$ on the properties of $Li_{1+x}Al_xTi_{2-x}(PO_4)_3$ (x = 0; 0.3), Solid State Ionics. 302 (2016) 49–53. https://doi.org/10.1016/j.ssi.2016.10.008.

[47] K. Waetzig, A. Rost, U. Langklotz, B. Matthey, J. Schilm, An explanation of the microcrack formation in $Li_{1.3}Al_{0.3}Ti_{1.7}(PO_4)_3$ ceramics, J. Eur. Ceram. Soc. 36 (2016) 1995–2001. https://doi.org/10.1016/j.jeurceramsoc.2016.02.042.

[48] B. Davaasuren, F. Tietz, Impact of sintering temperature on phase formation, microstructure, crystallinity and ionic conductivity of $Li_{1.5}Al_{0.5}Ti_{1.5}(PO_4)_3$, Solid State Ionics. 338 (2019) 144–152. https://doi.org/10.1016/j.ssi.2019.05.016.

[49] Z. Li, X. Zhao, Influence of Excess Lithium and Sintering on the Conductivity of $Li_{1.3}Al_{0.3}Ti_{1.7}(PO_4)_3$. *Funct. Mater. Lett.*, *12* (2019), 5–9. https://doi.org/10.1142/S1793604719500474.

[50] T. Hupfer, E.C. Bucharsky, K.G. Schell, A. Senyshyn, M. Monchak, M.J. Hoffmann, H. Ehrenberg, Evolution of microstructure and its relation to ionic conductivity in $Li_{1+x}Al_xTi_{2-x}(PO_4)_3$, Solid State Ionics. 288 (2016) 235–239. https://doi.org/10.1016/j.ssi.2016.01.036.

[51] S.D. Jackman, R.A. Cutler, Effect of microcracking on ionic conductivity in LATP, J. Power Sources. 218 (2012) 65–72. https://doi.org/10.1016/j.jpowsour.2012.06.081.

[52] C.A. Handwerker, J. E. Blendell, Ceramics : Grain Growth, Encycl. Mater. Sci. Technol. (2001) 1105–1108.

[53] A. Robertson, J. G. Fletcher, J. M. S. Skakle, A. R. West, Synthesis of $LiTiPO_5$ and $LiTiAsO_5$ with the α-Fe_2PO_5 Structure. *Journal of Solid State Chemistry*., (1994) 53–59. https://doi.org/10.1006/jssc.1994.1070.

[54] J. Fu, Superionic conductivity of glass-ceramics in the system Li_2O-Al_2O_3-TiO_2-P_2O_5, Solid State Ionics. 96 (1997) 195–200. https://doi.org/10.1016/s0167-2738(97)00018-0.

[55] E. Zhao, F. Ma, Y. Jin, K. Kanamura, Pechini synthesis of high ionic conductivity $Li_{1.3}Al_{0.3}Ti_{1.7}(PO_4)_3$ solid electrolytes: The effect of dispersant, J. Alloys Compd. 680 (2016) 646–653. https://doi.org/10.1016/j.jallcom.2016.04.173.

[56] E. Zhao, F. Ma, Y. Guo, Y. Jin, Stable LATP/LAGP double-layer solid electrolyte prepared: Via a simple dry-pressing method for solid state lithium ion batteries, RSC Adv. 6 (2016) 92579–92585. https://doi.org/10.1039/c6ra19415j.

[57] J.T.S. Irvine, D.C. Sinclair, A.R. West, Electroceramics: Characterization by Impedance Spectroscopy, Adv. Mater. 2 (1990) 132–138. https://doi.org/10.1002/adma.19900020304.

[58] K. Kwatek, W. Ślubowska, J. Trébosc, O. Lafon, J.L. Nowiński, Structural and electrical

properties of ceramic Li-ion conductors based on $Li_{1.3}Al_{0.3}Ti_{1.7}(PO_4)_3$-LiF, J. Eur. Ceram. Soc. 40 (2020) 85–93. https://doi.org/10.1016/j.jeurceramsoc.2019.08.032.

[59] J. Zhang, T. Kozawa, X. Li, H. Bai, J. Hu, F. Shao, M. Naito, Y. Duan, Influence of $LiBO_2$ addition on the microstructure and lithium-ion conductivity of $Li_{1+x}Al_xTi_{2-x}(PO_4)_3$ (x = 0.3) ceramic electrolyte, Ceram. Int. 44 (2018) 6558–6563. https://doi.org/10.1016/j.ceramint.2018.01.058.

[60] D. C. Gunduz, R. Schierholz, S. Yu, H. Tempel, H. Kungl, R.-A. Eichel, Combined quantitative microscopy on the microstructure and phase evolution in $Li_{1.3}Al_{0.3}Ti_{1.7}(PO_4)_3$ ceramics. Journal of Advanced Ceramics, 9(2020) 1–13. https://doi.org/10.1007/s40145-019-0354-0.

[61] M. Gellert, K.I. Gries, C. Yada, F. Rosciano, K. Volz, B. Roling, Grain boundaries in a lithium aluminum titanium phosphate-type fast lithium ion conducting glass ceramic: Microstructure and nonlinear ion transport properties, J. Phys. Chem. C. 116 (2012) 22675–22678. https://doi.org/10.1021/jp305309r.